Tunneling of Transverse Acoustic Waves on a Silicon Chip

Nicolas P. Mauranyapin,[*,†] Erick Romero,[†] Rachpon Kalra, Glen Harris, Christopher G. Baker, and Warwick P. Bowen

ARC Centre for Engineered Quantum Systems, School of Mathematics and Physics, The University of Queensland, Brisbane, Queensland 4072, Australia

(Received 12 January 2021; revised 8 April 2021; accepted 16 April 2021; published 17 May 2021)

Nanomechanical circuits for transverse acoustic waves promise to enable new approaches to computing, precision biochemical sensing, and many other applications. However, progress is hampered by the lack of precise control of the coupling between nanomechanical elements. Here, we demonstrate virtual-phonon coupling between transverse mechanical elements, exploiting tunneling through a zero-mode acoustic barrier. This allows the construction of large-scale nanomechanical circuits on a silicon chip, for which we develop a scalable fabrication technique. As example applications, we build mode-selective acoustic mirrors with controllable reflectivity and demonstrate acoustic spatial-mode filtering. Our work paves the way toward applications such as fully nanomechanical computer processors and distributed nanomechanical sensors, and exploration of the rich landscape of nonlinear nanomechanical dynamics.

DOI: 10.1103/PhysRevApplied.15.054036

I. INTRODUCTION

Large-scale nanomechanical circuits promise diverse applications, from heat mitigation in next-generation computer architectures [1] to integrated nanomechanical sensor arrays for biomedical diagnostics [2], nanomechanical computers robust to ionizing radiation [3] and quantum information processing and storage technologies [4–8]. Transverse nanomechanical circuits are particularly important. They dominate applications in nanomechanical sensing and computing [9] and in nonlinear dynamics [10], due to the orders-of-magnitude higher sensitivity and nonlinearity that can be provided by transverse acoustic waves (see the Supplemental Material [11]). However, progress has been slowed by a lack of effective means to couple acoustic energy between transverse nanomechanical elements. As a result, most transverse nanomechanical circuits created to date have employed only a few elements [12].

Transverse nanomechanical coupling is conventionally achieved via an effective spring interaction, as illustrated in Fig. 1(a). For instance, pairs of nanomechanical resonators can be spring coupled directly using a tether [13–15] or indirectly through their mutual interaction with a common substrate [16]. Acoustic phonons then couple from one element to the next through the intermediary spring. However, resonances in the spring capture acoustic energy and create complex frequency dependence, while the long range of the coupling necessitates large device footprints that are impractical for many applications (see the Supplemental Material [11]).

In this paper, we implement a fundamentally different form of transverse-wave coupling, where energy is transferred by virtual phonons [Fig. 1(b)]. To achieve this, we develop an architecture for nanomechanical circuitry based on sequences of zero-mode, single-mode, and multimode acoustic waveguides. We show that transverse acoustic waves tunnel through the zero-mode waveguides, which act as tunnel barriers in which only virtual phonons can exist. The tunnel barriers exhibit no resonances due to the absence of real phonons, while the exponential decay of the acoustic excitation within them allows compact device footprints.

Our architecture is CMOS compatible, allowing the construction of complex nanomechanical devices from a pattern of subwavelength-scale holes in a thin membrane. As example applications, we demonstrate mode-selective acoustic mirrors and spatial-mode filters on a silicon chip—capabilities required for spatial-mode multiplexing and mode cleaning in phononic circuits. Together, our results provide a pathway for scalable transverse nanomechanical circuitry, with broad applications from distributed sensing to nonlinear phononics.

II. THEORY

The devices developed here are made from a thin (approximately 80-nm) highly stressed silicon nitride (Si_3N_4) membrane, grown upon a silicon (Si) wafer. Once released from the silicon, these membranes support acoustic waves with motion predominantly in the out-of-plane

*n.mauranyapin@uq.edu.au

†These authors contributed equally to this work.

 © 2021 American Physical Society

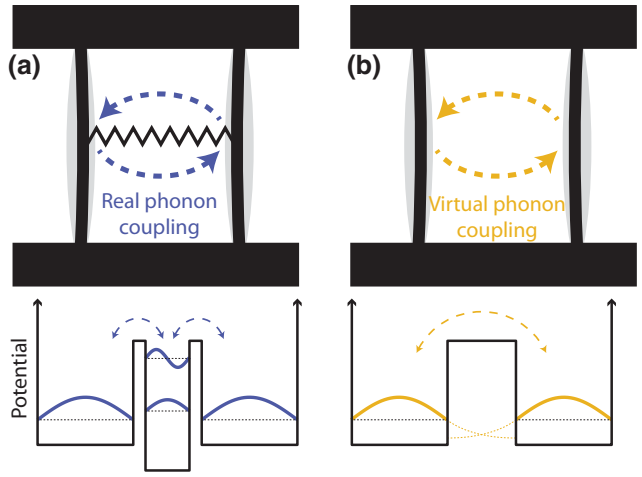

FIG. 1. Coupling types. (a) Spring coupling. (b) Virtual phonon coupling. Top, schematics of two mechanical elements represented by doubled clamped beams coupled via real [case (a)] or virtual [case (b)] phonons. Bottom, the corresponding potential energy landscape as a function of position. In case (a), real phonons couple in and out of the spring via allowed states. However, in case (b), the absence of modes results in acoustic tunneling by virtual phonons.

direction [17] [the z direction in Fig. 2(a)]. The membrane motion obeys a standard two-dimensional (2D) wave equation (see Ref. [17]) with dispersion relation

$$\Omega = \sqrt{\frac{\sigma}{\rho}}\sqrt{k_y^2 + \left(\frac{n\pi}{L_x}\right)^2}, \tag{1}$$

where Ω is the angular frequency of the acoustic wave excitation, σ is the tensile stress of the membrane, ρ is the density of the membrane material, k_y is the wave number in the direction of propagation, L_x is the width of the waveguide in the transverse direction, and n is an integer representing the transverse mode number. From this equation, one can see that each mode has a cutoff frequency,

$$\Omega_{c,n} = \sqrt{\frac{\sigma}{\rho}}\left(\frac{n\pi}{L_x}\right), \tag{2}$$

below which the wave number k_y is imaginary. Therefore, if the mode n is excited at a frequency below $\Omega_{c,n}$, there is no real wave vector available in the dispersion relation and the amplitude of the acoustic wave will decay exponentially over distance. Such evanescent waves are associated to the presence of virtual phonons, as opposed to real phonons, which are associated with propagating acoustic waves (see Fig. 1). Thus, there will be a range of frequencies ($\Omega < \Omega_{c,1}$) where no mode can propagate, followed by a range of frequencies ($\Omega_{c,1} < \Omega < \Omega_{c,2}$) where only the first transverse mode is allowed and the system is single mode [17]. This is the physical phenomenon that will be leveraged in this paper to engineer acoustic tunneling.

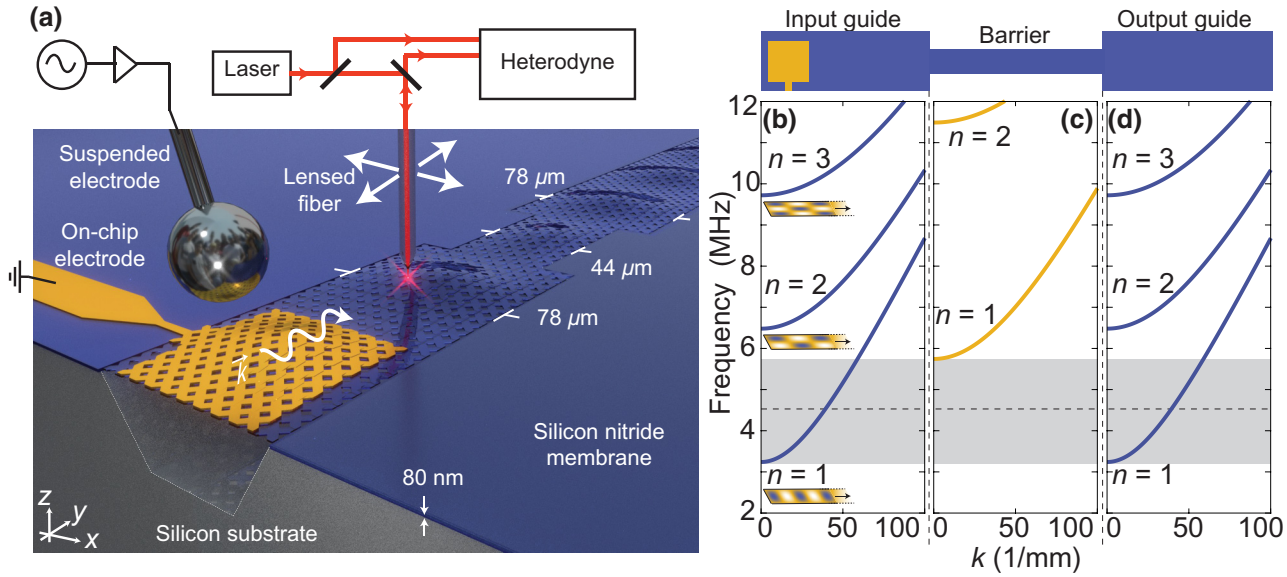

FIG. 2. The experimental setup and dispersion relation. (a) The phononic device consists of an input waveguide, a tunnel barrier, and an output waveguide made out of an approximately 80-nm-thick released silicon nitride membrane. Mechanical waves are excited via electrostatic forces between a suspended and an on-chip electrode separated by approximately 2 μm (left). The mechanical vibrations are detected using heterodyne interferometry (right). (b)–(d) The phononic dispersion relations of the input waveguide, barrier, and output waveguide, respectively, calculated from Eq. (1). Mode profiles calculated from the solutions of the wave equation are shown as inset images in (b) for the first three modes ($n = 1, 2, 3$). The gray shaded region in (b)–(d) indicates the frequency band within the single-mode tunneling regime.

Above the second transverse-mode cutoff frequency, $\Omega > \Omega_{c,2}$, the membrane can support several acoustic modes and becomes multimode.

We design phononic devices, as shown in Fig. 2(a), composed of an input waveguide connected to a narrower-width waveguide section (referred to henceforth as the "tunnel barrier"), itself connected to an output waveguide of the same width as the input waveguide. Since the dispersion relation depends on the width of the waveguide, the input and output waveguides have different dispersion relations to that of the tunnel barrier, as displayed in Figs. 2(b)–2(d). This leads to different first-mode cutoff frequencies ($\Omega_{c,1}^{\text{guides}}$ and $\Omega_{c,1}^{\text{barrier}}$) and to different operating regimes, depending on the excitation frequency Ω.

If $\Omega_{c,1}^{\text{guide}} < \Omega < \Omega_{c,1}^{\text{barrier}}$ the acoustic wave can propagate in the guides via its first transverse mode but decays exponentially in the tunnel barrier, partially reflecting and partially tunneling into the output waveguide. We henceforth refer to this range of frequencies, where the device acts as an acoustic mirror with controllable reflectivity, as the "single-mode tunneling regime." The ratio of reflection to tunneling depends on the magnitude of the exponential decay and therefore on both the length of the tunnel barrier and the amplitude exponential decay length γ. For frequencies within the single-mode tunneling regime, γ is given by

$$\gamma = \left[\left(\frac{\pi}{L_x}\right)^2 - \Omega^2\frac{\rho}{\sigma}\right]^{-1/2}. \tag{3}$$

Thus, the strength of the coupling between the two waveguides can be engineered by carefully choosing the length of the tunnel barrier or the driving frequency. The closer the frequency to $\Omega_{c,1}^{\text{barrier}}$, the stronger is the coupling. Indeed, as $\Omega_{c,1}^{\text{barrier}}$ is approached, the decay length of the wave approaches infinity, so that the acoustic wave is barely attenuated. On the other hand, at frequencies close to $\Omega_{c,1}^{\text{guide}}$ the decay length reaches a minimum of $\left[(\pi/L_x^{\text{barrier}})^2 - (\pi/L_x^{\text{guide}})^2\right]^{-1/2}$, leading to maximal attenuation.

III. MESHED MECHANICAL SYSTEMS

Previously, processes used to fabricate membrane-based phononic devices have relied either on deep-backside etching [17,18] or on the use of wavelength-scale holes in the membrane to enable front-side etching [19,20]. For backside etching processes, the need to etch through a several-hundred-micron-thick substrate has limited both the precision and the feature size of the phononic components, while in the case of front-side etching, the wavelength-scale hole pattern [10,21,22] directly affects the dispersion relations of the guided modes and limits the ability to fabricate arbitrary waveguide shapes.

Here, we develop a fabrication platform that overcomes these two issues. It is based on a far-subwavelength hole pattern, resulting in a "meshed" silicon nitride membrane through which the underlying silicon substrate can be etched away from the front side. The pattern consists of square holes of 1 μm by 1 μm, periodically separated (center to center) by 2 μm [see Fig. 3(a)]. These lengths are approximately 2 orders of magnitude smaller than the typical wavelengths of the guided acoustic waves. Therefore, the interaction of the supported acoustic waves with the holes is expected to be greatly suppressed, leaving the dispersion relation Eq. (1) essentially unaffected, with only the ratio $\sqrt{\sigma/\rho}$ reduced by 10% compared to a nonpatterned membrane (see Appendix A and the Supplemental Material [11]). This is verified through finite-element simulations of the $n = 1$ and $n = 2$ transverse modes of a meshed membranes [displayed in Fig. 3(b)], which show no apparent differences in mode shape from the corresponding acoustic waves propagating on a nonpatterned membrane.

The meshed phononic devices are fabricated on a chip from a commercial wafer with an approximately 80-nm stoichiometric Si_3N_4 film (LPCVD deposition, initial tensile stress $\sigma_0 = 1$ GPa) deposited on a silicon substrate. The hole pattern in the silicon nitride membrane is defined through a combination of electron-beam lithography and reactive ion etching. The devices are released through anisotropic wet etching of the underlying silicon using a potassium hydroxide (KOH) solution. Alignment of the waveguides along the [011] crystal axis results in near atomically smooth side walls [see Fig. 3(c) and Appendix B].

An optical image of the phononic device is shown in Fig. 3(d), with the colors of different layers arising naturally due to the thin-film interference effects. The yellow, red, and blue frames, respectively, enclose the on-chip electrode, the tunnel barrier, and the end of the output waveguide. Scanning electron images of these regions are shown in Figs. 3(e)–3(g), respectively. One can see the straight planar side walls closely following the pattern of holes and that features smaller than 10 μm can be achieved in the released membrane using this technique. Despite the high initial tensile stress, the process is remarkably robust, generally achieving yields of 100% for chips containing as many as 48 devices.

IV. SETUP

We fabricate devices with input and output waveguide widths of $L_x = 78$ μm and a tunnel barrier width of $L_x = 44$ μm. The input and output waveguides are approximately 1 mm long in the direction of propagation and different tunnel barrier lengths are investigated. Given the choice of widths, the cutoff frequency of the first mode of the guides and the tunnel barrier are found from Eq. (2)

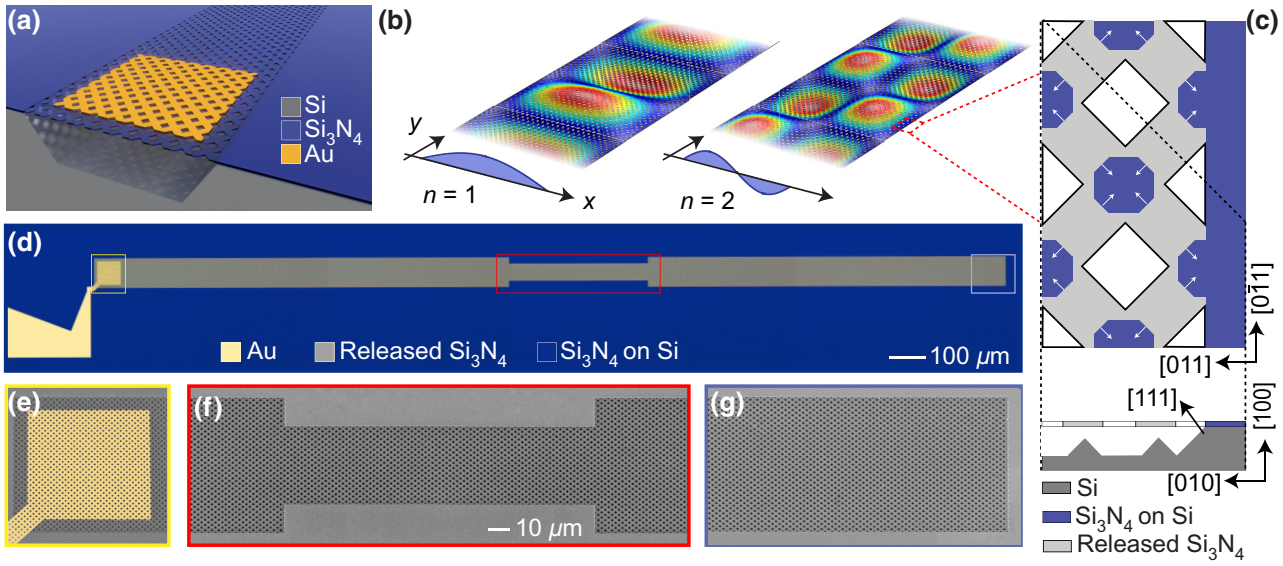

FIG. 3. The meshed-phononic-waveguide fabrication. (a) A schematic of the meshed silicon nitride membrane released from the silicon substrate and the gold actuation electrode. (b) Finite-element simulations showing the transverse mode profile of the first ($n = 1$) and second ($n = 2$) acoustic modes of a meshed waveguide. (c) A schematic of a snapshot of the chip during the KOH etch. The top figure is a top view of the chip and the mesh pattern in shown in white; the released silicon nitride is displayed in light gray and the nonreleased membrane in blue. The bottom figure is a cut of the top figure along the black dashed line. (d) An optical microscope image showing the input waveguide with a meshed gold electrode (yellow square), the tunnel barrier (red rectangle), and the output waveguide (blue rectangle). (e)–(g) False-color scanning electron micrograph of the actuation region with a gold electrode, the tunnel barrier, and the end of the output waveguide, respectively.

to be $\Omega_{c,1}^{\text{guide}}/2\pi = 3.2$ MHz and $\Omega_{c,1}^{\text{barrier}}/2\pi = 5.6$ MHz, respectively. This provides a frequency band of 2.4 MHz (gray shading in Figs. 2(b)–2(d)] for which single-mode acoustic tunneling can be investigated.

Acoustic waves are launched into the device through electrostatic actuation [17] between a gold electrode patterned on the input waveguide and a suspended electrode, as shown in Fig. 2(a). To detect the motion of the membrane, we use an optical lensed fiber combined with heterodyne detection (for more details, see Refs. [17,23]). Once detected, the heterodyne signal produces a photocurrent whose amplitude is proportional to the amplitude of the membrane motion at the point of focus of the lensed fiber. Therefore, by scanning the lensed fiber across and along the device, we can determine the amplitude of an acoustic wave at any position.

V. RESULTS

A. Exponential decay

We first investigate how the acoustic wave decays in the tunnel barrier. To do this, we use a device with a 150-μm-long tunnel barrier, significantly longer than the typical acoustic wave decay length in the barrier. To investigate the response of the device, we perform a network analysis with the lensed fiber placed in the middle (both in the x and y directions) of the input waveguide [see Fig. 4(a), red dot]. The results are displayed in Fig. 4(b) and we observe no response from the device at frequencies below approximately 3.5 MHz, consistent with the theoretical cutoff frequency of the waveguide of 3.2 MHz. Above this frequency, we observe a series of resonant peaks. These peaks are expected due to the finite dimensions of the device, with impedance mismatch between the released silicon nitride membrane and the silicon substrate causing reflection of the acoustic wave at each end of the input waveguide [17].

The quality factors of the observed resonances can be used to provide an upper bound on the losses of the acoustic wave during propagation [17]. We observe quality factors as high as 5000. This corresponds to a loss per unit length as low as 0.4 dB cm^{-1}. This indicates an absence of additional damping introduced by the subwavelength mesh used for fabrication.

We use the amplitude enhancement provided by these resonances to investigate how the acoustic wave decays in the tunnel barrier. To do so, the device is continuously driven at one of the resonance frequencies within the single-mode tunneling regime while the lensed fiber is scanned in the y direction along the input waveguide and the tunnel barrier at the x position $x = L_x/2$ [see Fig. 4(a)]. The amplitude of the membrane motion is recorded continuously over the scanning distance.

A typical scan is shown in Fig. 4(c) for a driving frequency of 4.9 MHz. The power of the acoustic wave

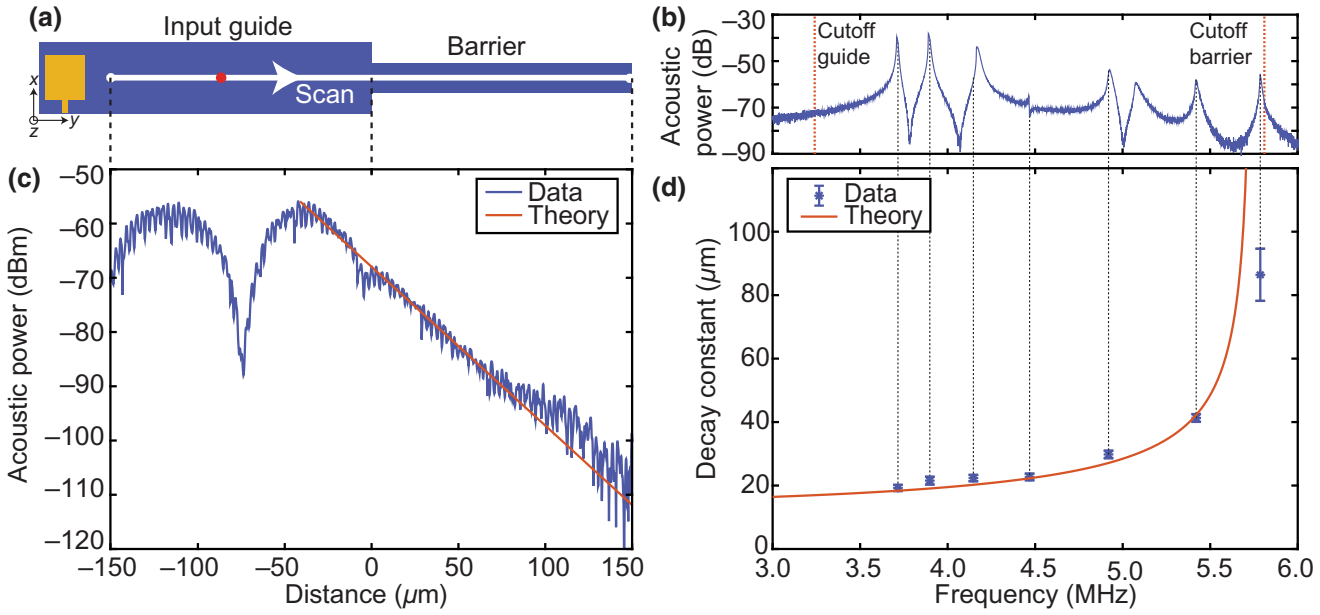

FIG. 4. The exponential decay. (a) The scheme of the one-dimensional (1D) scan. The lensed fiber is scanned from the input waveguide until the end of the tunnel barrier at $x = 0.5L_x$ at a rate of ten steps per second, with a step size varying from scan to scan between 880 and 900 nm. The amplitude of the mechanical signal is recorded on a spectrum analyser at zero span and 10-Hz resolution bandwidth. (b) Network analysis performed in the middle of the input waveguide [$x = 0.5L_x$ and $y = 0.5L_y$ represented by the red dot in (a)]. The cutoff frequency of the waveguide and tunnel barrier first mode are displayed in red and calculated using the equations from the theoretical discussed previously. (c) An experimental scan of the input waveguide and tunnel barrier (150 μm long). The power of the acoustic wave is displayed versus the scanning distance for a typical scan at a driving frequency of 4.9 MHz. The fast periodic modulations on the trace originate from the mesh pattering of the waveguide, which modulates the reflection of the probing optical beam. The theoretical prediction in red is calculated from the amplitude of the wave at the guide–tunnel-barrier interface (distance axis = 0 μm), with no fitting parameter. (d) The extracted evanescent decay constant versus the drive frequency measured at the points in (b) indicated by the dashed lines. The error bars are calculated from the standard deviation over six different scans for each frequency. The red theoretical line is obtained from Eq. (3), with no fitting parameter.

is plotted versus the distance scanned by the fiber along the direction of propagation. The coordinate $y = 0$ corresponds to the junction between the input waveguide and the tunnel barrier. One can see that, for $y > 0$, the acoustic wave amplitude decays exponentially in the tunnel barrier, as expected for this frequency. For $y < 0$, we observe standing-wave oscillations, as expected due to the resonant nature of the input waveguide. The red line in Fig. 4(c) corresponds to the theoretical decay expected for an acoustic wave at frequency 4.9 MHz. The good agreement with the experimental data verifies that the simple theoretical model discussed previously is appropriate for our experimentally fabricated devices.

To map the dependence of γ with the drive frequency, this process is repeated for seven different drive frequencies [corresponding to the peaks shown in Fig. 4(b)]. The results are shown in Fig. 4(d) and compared to the theoretical prediction of Eq. (3), without any fitting parameters. As expected, the decay length increases with the frequency and tends to infinity as the cutoff frequency of the first mode of the tunnel barrier is approached. This experimentally demonstrates that varying the drive frequency provides the ability to tune the decay length by more than a factor of 4. The good agreement with theory demonstrates that the phononic decay can be precisely and reliably engineered, opening a path toward scalable phononic circuitry.

B. Imaging acoustic tunneling

By raster scanning the lensed fiber in both the x and y directions as shown in Fig. 5(a), 2D images of the acoustic wave are recorded. Figures 5(b) and 5(c) display 2D scans of two different devices. In Fig. 5(b), the device has a tunnel barrier of length 150 μm and the image is recorded for a driving frequency of 5.4 MHz. As discussed previously but now in two dimensions, we observe a resonant wave in the input waveguide that exponentially decays below the noise floor in the tunnel barrier with the acoustic wave fully reflected. This is expected at this frequency because the decay length of the wave is around 42 μm [see Fig. 4(d)], which is three times smaller than the tunnel-barrier length.

The second device [Fig. 5(c)] has a shorter 75-μm-long tunnel barrier and is driven at a frequency of 5.5 MHz. We observe resonance in the input waveguide, then a

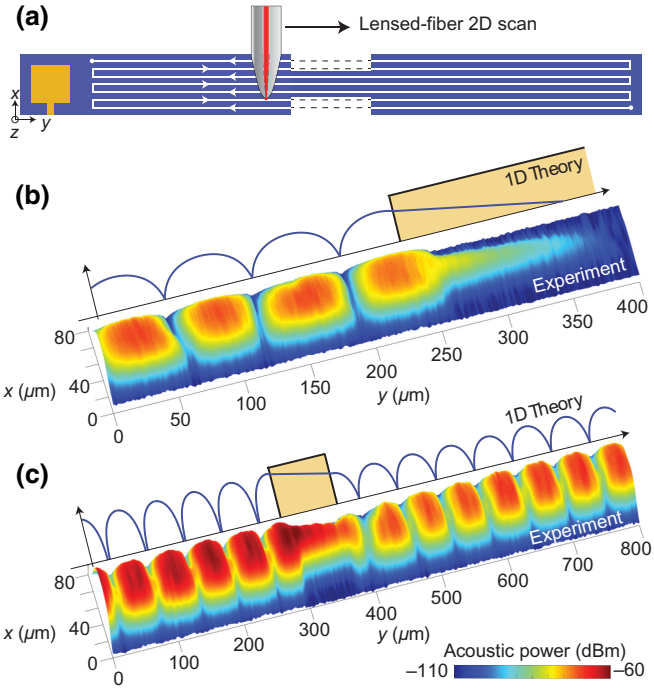

FIG. 5. Imaging of the acoustic decay and of tunneling. (a) A schematic of the experimental raster-scan imaging process where the lensed fiber is scanned in the y direction for several x positions. The different scans for all the x positions are assembled in postprocessing. (b) Imaging of the exponential acoustic decay in a device with a 150-μm-long tunnel barrier. The device is continuously driven at 4.9 MHz while imaging. The top schematics show a theoretical prediction of acoustic exponential decay in one dimension. (c) Imaging of the acoustic tunneling. The device is driven at 5.5 MHz and has a 75-μm-long tunnel barrier. The experimental data in (b) and (c) are smoothed with a Gaussian filter.

short exponential decay in the tunnel barrier, followed by resonant buildup again in the output waveguide. Overall, we observe transmission through the tunnel barrier of 10% via virtual phonon coupling, similar to the frustrated total internal reflection observed between two prisms in photonics [24].

C. Acoustic mode filtering

To illustrate one application of the ability to engineer acoustic wave tunneling, we consider acoustic spatial-mode filtering, which is an important capability for phononic circuitry. Similarly to photonics, it allows spatial-mode multiplexing, control of spatial dispersion, and filtering of scattering from defects [25], among other prospective applications. Here, we demonstrate it by arranging a scenario where both guides can support the first two transverse modes but the tunnel barrier remains in the single-mode regime. In this case, if both modes are excited in the input waveguide, only the first transverse mode will be allowed to transmit through the barrier into the output waveguide, with the second mode fully reflected.

This regime can be achieved by driving the device at frequencies below the second-mode cutoff frequency of the barrier $\Omega_{c,2}^{\text{barrier}}/2\pi = 11.5$ MHz and between the second- and third-mode cutoff frequencies of the waveguides, $\Omega_{c,2}^{\text{guide}}/2\pi = 6.5$ MHz and $\Omega_{c,3}^{\text{guide}}/2\pi = 9.7$ MHz, respectively. Figures 6(a) and 6(b) show theoretical predictions of the propagation of the first and second acoustic modes in the waveguides, respectively. If both modes are driven simultaneously, they will interfere, creating spatial patterns such as shown in Fig. 6(c). Choosing a 8.1-MHz excitation frequency, the decay length of the second mode is estimated [using Eq. (3)], adapted for the second transverse mode), to be around 7 μm. After a 75-μm-long

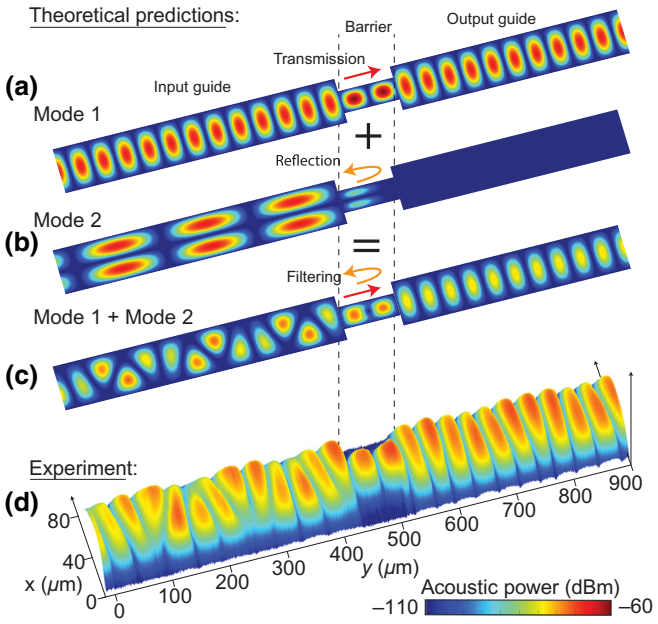

FIG. 6. Acoustic mode filtering. (a)–(c) Theoretical predictions of the acoustic power of a device driven at a frequency between the second- and third-mode cutoff frequencies ($\Omega_{c,2}^{\text{guide}} < \Omega < \Omega_{c,3}^{\text{guide}}$) of the guide. (a) The acoustic power if only the first mode is excited and (b) if only the second mode is excited for the same frequency: (c) corresponds to the interference pattern of the first two modes with identical amplitudes and is calculated by summing (a) and (b) over the entire device. (d) The experimental imaging of a device with a 75-μm-long tunnel barrier driven at 8.1 MHz experimentally, showing acoustic mode filtering. We believe that both modes can be excited simultaneously in the input waveguide because the on-chip electrode is not symmetric in the propagation direction. Note that in this configuration, resonances in the output waveguide can cause enhancement or suppression of the amplitude of the transmitted waves. Due to these effects, we find that it is not possible to experimentally quantify the suppression of the second mode due only to the tunnel barrier. The experimental data are smoothed with a Gaussian filter.

tunnel barrier, this is predicted to exponentially reduce the power in the second mode by a factor of 2×10^9 (or -93 dB). The first mode, on the other hand, passes essentially unaffected. We then expect that the second transverse mode will be spatially filtered by the device. Figure 6(d) shows an experimental image of the acoustic propagation in this configuration. The results are consistent with the theory, showing clear acoustic mode filtering.

VI. DISCUSSION AND CONCLUSIONS

Transverse nanomechanical circuits have many potential applications [1–8]. However, the inability to effectively couple transverse nanomechanical elements has slowed progress, limiting circuits to simple configurations of a few components [12]. Our work aims to provide a resolution to this issue, introducing a coupling method based on acoustic tunneling and demonstrating that it can be used to construct mode-selective acoustic mirrors and acoustic mode filters. The absence of propagating modes within the coupler removes the resonances intrinsic to other methods [26] (see the Supplemental Material [11]). This greatly suppresses energy capture inside the coupler and significantly increases tolerance to fabrication imperfections. Tunneling also greatly reduces the length scale over which coupling occurs, providing the possibility of orders-of-magnitude reduced device footprints compared to other single-layer devices (see the Supplemental Material [11]).

To observe tunneling, we report the development of a scalable silicon-chip-based architecture for nanomechanical circuitry, which we construct using a CMOS-compatible fabrication approach. The architecture is based on zero-mode tunnel barriers, within which only virtual phonons can exist, integrated with single- and multimode acoustic waveguides. This guide-barrier approach is analogous to evanescent coupling in optics [27], which has, for example, been used to build complex photonic circuits [28], spatial filters [29], add-drop filters [30], and coupled resonators [31]. As in photonics, the use of single-mode waveguides offers immunity to deleterious effects such as modal dispersion, spatial-mode mismatch, and scattering from defects.

Acoustic tunneling has been demonstrated for longitudinal acoustic waves in the 1970s [32] and has recently been exploited to build basic nanomechanical circuits [7,8]. Phonon dimers have also recently been reported [33]. Our work builds on these results, showing that transverse tunneling can be used to couple elements for nanomechanics circuitry. Transverse waves dominate applications in areas such as nanomechanical sensing, computing, and nonlinear mechanics [9,13]. For instance, they provide 4-orders-of-magnitude improved precision in nanomechanical mass sensing [34] and 2-orders-of-magnitude higher mechanical nonlinearity (see the Supplemental Material [11]). We therefore expect the results presented here to open up diverse applications from distributed sensing to quantum information and nanomechanical computing.

ACKNOWLEDGMENTS

This work was performed in part at the Queensland node of the Australian National Fabrication Facility, a company established under the National Collaborative Research Infrastructure Strategy to provide nano- and microfabrication facilities for Australia's researchers. We acknowledge the facilities, and the scientific and technical assistance, of the Australian Microscopy & Microanalysis Research Facility at the Centre for Microscopy and Microanalysis, The University of Queensland. We thank Elliot Cheng and Tihan Bekker for their help for the fabrication and their comments on the manuscript. This research was primarily funded by the Australian Research Council and the Lockheed Martin Corporation through the Australian Research Council Linkage Grant No. LP160101616. Support was also provided by the Australian Research Council Centre of Excellence for Engineered Quantum Systems (Grant No. CE170100009). R.K., C.G.B., and W.P.B. acknowledge fellowships from The University of Queensland (Grant No. UQFEL1719237) and the Australian Research Council (Grants No. DE190100318 and No. FT140100650), respectively.

APPENDIX A: MESH MEMBRANE PARAMETERS

Compared to a typical nonpatterned membrane, the mesh on the silicon nitride has two main effects: it decreases the density of the membrane and it decreases the average stress because the membrane relaxes. This modifies the velocity of guided waves. Since the wave velocity is defined as $v = \sqrt{\sigma/\rho}$, a decrease of density will increase v, while a decrease of stress will decrease v. Our simulations indicate that the change in stress dominates, resulting in a reduction of wave velocity by a factor of 0.9 (see the Supplemental Material [11]). The mass of our meshed membrane is reduced by a factor of 3/4 (see Fig. 3(c) and the Supplemental Material [11]): with the density of the silicon nitride $\rho_0 = 3200$ kg/m^3, we obtain $\rho = (3/4)\rho_0 = 2400$ kg/m^3 and $\sigma \sim 0.61\sigma_0 = 0.61$ GPa with $\sigma_0 = 1$ GPa.

APPENDIX B: MESH MEMBRANE FABRICATION PROCESS

The electrodes are patterned using electron-beam lithography on a double layer of polymethyl methacrylate (PMMA) resist, followed by 50 nm of gold evaporation and lift-off. The mesh array is aligned to the gold electrodes and patterned using AR-P electron-beam resist. The mesh is formed by etching the exposed Si_3N_4 film using reactive ion etching with a plasma of CHF_3 and SF_6. The AR-P resist is then stripped off with oxygen plasma. The

underlying silicon is removed using a solution of low-concentration potassium hydroxide (KOH) combined with isopropyl alcohol until the membrane is released, as represented in Fig. 3(c). The chip is dried in a CO_2 critical-point dryer.

APPENDIX C: EXPERIMENTAL PARAMETERS

To mechanically drive the device, a signal generator at frequency $\Omega/2\pi$ and 0 dBm power is connected to a 30 V dc supply, amplified by 25 dBm, and sent to the suspended electrode approximately 2μm above the gold on-chip electrode, to generate acoustic waves via electrostatic forces.

The experiments are performed in a high-vacuum chamber (pressure 10^{-7} mbar) to eliminate any air damping of the membrane motion [35].

[1] K. Biswas, J. He, I. D. Blum, C.-I. Wu, T. P. Hogan, D. N. Seidman, V. P. Dravid, and M. G. Kanatzidis, High-performance bulk thermoelectrics with all-scale hierarchical architectures, Nature **489**, 414 (2012).

[2] M. K. Baller, H. P. Lang, J. Fritz, C. Gerber, J. K. Gimzewski, U. Drechsler, H. Rothuizen, M. Despont, P. Vettiger, and F. Battiston *et al.*, A cantilever array-based artificial nose, Ultramicroscopy **82**, 1 (2000).

[3] G. Furano, R. Jansen, and A. Menicucci, Review of radiation hard electronics activities at European Space Agency, J. Instrum. **8**, C02007 (2013).

[4] M. Pechal, P. Arrangoiz-Arriola, and A. H. Safavi-Naeini, Superconducting circuit quantum computing with nanomechanical resonators as storage, Quantum Sci. Technol. **4**, 015006 (2018).

[5] A. Bienfait, K. J. Satzinger, Y. Zhong, H.-S. Chang, M.-H. Chou, C. R. Conner, É. Dumur, J. Grebel, G. A. Peairs, and R. G. Povey *et al.*, Phonon-mediated quantum state transfer and remote qubit entanglement, Science **364**, 368 (2019).

[6] K. J. Satzinger, Y. Zhong, H.-S. Chang, G. A. Peairs, A. Bienfait, M.-H. Chou, A. Cleland, C. R. Conner, É. Dumur, and J. Grebel *et al.*, Quantum control of surface acoustic-wave phonons, Nature **563**, 661 (2018).

[7] H. Shin, J. A. Cox, R. Jarecki, A. Starbuck, Z. Wang, and P. T. Rakich, Control of coherent information via on-chip photonic-phononic emitter-receivers, Nat. Commun. **6**, 6427 (2015).

[8] W. Fu, Z. Shen, Y. Xu, C.-L. Zou, R. Cheng, X. Han, and H. X. Tang, Phononic integrated circuitry and spin-orbit interaction of phonons, Nat. Commun. **10**, 1 (2019).

[9] G. Longo, L. Alonso-Sarduy, L. M. Rio, A. Bizzini, A. Trampuz, J. Notz, G. Dietler, and S. Kasas, Rapid detection of bacterial resistance to antibiotics using AFM cantilevers as nanomechanical sensors, Nat. Nanotechnol. **8**, 522 (2013).

[10] M. Kurosu, D. Hatanaka, K. Onomitsu, and H. Yamaguchi, On-chip temporal focusing of elastic waves in a phononic crystal waveguide, Nat. Commun. **9**, 1331 (2018).

[11] See the Supplemental Material at http://link.aps.org/supplemental/10.1103/PhysRevApplied.15.054036 for further the information which includes references [36–46].

[12] J.-S. Wenzler, T. Dunn, T. Toffoli, and P. Mohanty, A nanomechanical Fredkin gate, Nano Lett. **14**, 89 (2014).

[13] S. Lee and C.-C. Nguyen, in *Proceedings of the 2004 IEEE International Frequency Control Symposium and Exposition, 2004.* (IEEE, Montreal, QC, Canada, 2004), p. 144.

[14] M. U. Demirci and C. T.-C. Nguyen, Mechanically corner-coupled square microresonator array for reduced series motional resistance, J. Microelectromech. Syst. **15**, 1419 (2006).

[15] D. S. Greywall and P. A. Busch, Coupled micromechanical drumhead resonators with practical application as electromechanical bandpass filters, J. Micromech. Microeng. **12**, 925 (2002).

[16] J. Doster, S. Hönl, H. Lorenz, P. Paulitschke, and E. M. Weig, Collective dynamics of strain-coupled nanomechanical pillar resonators, Nat. Commun. **10**, 1 (2019).

[17] E. Romero, R. Kalra, N. Mauranyapin, C. Baker, C. Meng, and W. Bowen, Propagation and Imaging of Mechanical Waves in a Highly Stressed Single-Mode Acoustic Waveguide, Phys. Rev. Appl. **11**, 064035 (2019).

[18] E. Romero, V. M. Valenzuela, A. R. Kermany, L. Sementilli, F. Iacopi, and W. P. Bowen, Engineering the Dissipation of Crystalline Micromechanical Resonators, Phys. Rev. Appl. **13**, 044007 (2020), Publisher: American Physical Society.

[19] D. Hatanaka, I. Mahboob, K. Onomitsu, and H. Yamaguchi, Phonon waveguides for electromechanical circuits, Nat. Nanotechnol. **9**, 520 (2014).

[20] J. Cha, K. W. Kim, and C. Daraio, Experimental realization of on-chip topological nanoelectromechanical metamaterials, Nature **564**, 229 (2018).

[21] M. Kurosu, D. Hatanaka, and H. Yamaguchi, Mechanical Kerr Nonlinearity of Wave Propagation in an On-Chip Nanoelectromechanical Waveguide, Phys. Rev. Appl. **13**, 014056 (2020).

[22] J. Cha and C. Daraio, Electrical tuning of elastic wave propagation in nanomechanical lattices at MHz frequencies, Nat. Nanotech **13**, 1016 (2018).

[23] N. Mauranyapin, L. Madsen, M. Taylor, M. Waleed, and W. Bowen, Evanescent single-molecule biosensing with quantum-limited precision, Nat. Photonics **11**, 477 (2017).

[24] A. Stahlhofen and G. Nimtz, Evanescent modes are virtual photons, EPL (Europhysics Letters) **76**, 189 (2006).

[25] L.-W. Luo, N. Ophir, C. P. Chen, L. H. Gabrielli, C. B. Poitras, K. Bergmen, and M. Lipson, WDM-compatible mode-division multiplexing on a silicon chip, Nat. Commun. **5**, 1 (2014).

[26] K. Fang, M. H. Matheny, X. Luan, and O. Painter, Optical transduction and routing of microwave phonons in cavity-optomechanical circuits, Nat. Photonics **10**, 489 (2016).

[27] H. A. Haus and W. Huang, Coupled-mode theory, Proc. IEEE **79**, 1505 (1991).

[28] Y. Tian, Z. Liu, H. Xiao, G. Zhao, G. Liu, J. Yang, J. Ding, L. Zhang, and L. Yang, Experimental demonstration of a reconfigurable electro-optic directed logic circuit using cascaded carrier-injection micro-ring resonators, Sci. Rep. **7**, 1 (2017).

[29] L. H. Gabrielli, J. Cardenas, C. B. Poitras, and M. Lipson, Silicon nanostructure cloak operating at optical frequencies, Nat. Photonics **3**, 461 (2009).
[30] Z. Qiang, W. Zhou, and R. A. Soref, Optical add-drop filters based on photonic crystal ring resonators, Opt. Express **15**, 1823 (2007).
[31] C. Bekker, C. G. Baker, R. Kalra, H.-H. Cheng, B.-B. Li, V. Prakash, and W. P. Bowen, Free spectral range electrical tuning of a high quality on-chip microcavity, Opt. Express **26**, 33649 (2018).
[32] V. Narayanamurti, H. Störmer, M. Chin, A. Gossard, and W. Wiegmann, Selective Transmission of High-Frequency Phonons by a Superlattice: The "Dielectric" Phonon Filter, Phys. Rev. Lett. **43**, 2012 (1979).
[33] L. Catalini, Y. Tsaturyan, and A. Schliesser, Soft-Clamped Phononic Dimers for Mechanical Sensing and Transduction, Phys. Rev. Appl. **14**, 014041 (2020).
[34] M. A. Taylor, A. Szorkovszky, J. Knittel, K. H. Lee, T. G. McRae, and W. P. Bowen, Cavity optoelectromechanical regenerative amplification, Opt. Express **20**, 12742 (2012).
[35] A. Naesby, S. Naserbakht, and A. Dantan, Effects of pressure on suspended micromechanical membrane arrays, Appl. Phys. Lett. **111**, 201103 (2017), Publisher: American Institute of Physics.
[36] S. Marquez, M. Álvarez, J. A. Plaza, L. Villanueva, C. Domínguez, and L. M. Lechuga, Asymmetrically coupled resonators for mass sensing, Appl. Phys. Lett. **111**, 113101 (2017).
[37] J. Košata, O. Zilberberg, C. L. Degen, R. Chitra, and A. Eichler, Spin Detection via Parametric Frequency Conversion in a Membrane Resonator, Phys. Rev. Appl. **14**, 014042 (2020).
[38] D. K. Shaeffer, Mems inertial sensors: A tutorial overview, IEEE Commun. Mag. **51**, 100 (2013).
[39] V. Kaajakari, T. Mattila, A. Oja, and H. Seppa, Nonlinear limits for single-crystal silicon microresonators, J. Microelectromech. Syst. **13**, 715 (2004).
[40] R. Lifshitz and M. Cross, Nonlinear dynamics of nanomechanical and micromechanical resonators, Rev. Nonlinear Dynamics Complexity **1**, 1 (2008).
[41] Y. L. Sfendla, C. G. Baker, G. I. Harris, L. Tian, R. A. Harrison, and W. P. Bowen, Extreme quantum nonlinearity in superfluid thin-film surface waves, Npj Quantum Inf. **7**, 1 (2021).
[42] V. Kaajakari, T. Mattila, A. Lipsanen, and A. Oja, Nonlinear mechanical effects in silicon longitudinal mode beam resonators, Sens. Actuators A: Phys. **120**, 64 (2005).
[43] J. Chaste, A. Eichler, J. Moser, G. Ceballos, R. Rurali, and A. Bachtold, A nanomechanical mass sensor with yoctogram resolution, Nat. Nanotechnol. **7**, 301 (2012).
[44] K. Ekinci, Y. Yang, and M. Roukes, Ultimate limits to inertial mass sensing based upon nanoelectromechanical systems, J. Appl. Phys. **95**, 2682 (2004).
[45] S. Schmid, L. G. Villanueva, and M. L. Roukes, *Fundamentals of Nanomechanical Resonators* (Springer, Cham, 2016), Vol. 49.
[46] S. K. Roy, V. T. Sauer, J. N. Westwood-Bachman, A. Venkatasubramanian, and W. K. Hiebert, Improving mechanical sensor performance through larger damping, Science **360**, eaar5220 (2018).